Title

Coupling morphological and magnetic anisotropy for assembling tetragonal colloidal crystals

Journal

Science Advances, 7(37)

ISSN

2375-2548

Authors

Li, Zhiwei

Qian, Chang

Xu, Wenjing

et al.

Publication Date

2021-09-10

DOI

10.1126/sciadv.abh1289

APPLIED SCIENCES AND ENGINEERING

Coupling morphological and magnetic anisotropy for assembling tetragonal colloidal crystals

Zhiwei Li[1], Chang Qian[1†], Wenjing Xu[1], Chenhui Zhu[2], Yadong Yin[1]*

Morphological and magnetic anisotropy can be combined in colloidal assembly to create unconventional secondary structures. We show here that magnetite nanorods interact along a critical angle, depending on their aspect ratios and assemble into body-centered tetragonal colloidal crystals. Under a magnetic field, size-dependent attractive and repulsive domains develop on the ends and center of the nanorods, respectively. Our joint experiment-computational multiscale study demonstrates the presence of a critical angle in the attractive domain, which defines the equilibrium bonding states of interacting rods and leads to the formation of non–close-packed yet hard-contact tetragonal crystals. Small-angle x-ray scattering measurement attributes the perfect tetragonal phase to the slow assembly kinetics. The crystals exhibit brilliant structural colors, which can be actively tuned by changing the magnetic field direction. These highly ordered frameworks and well-defined three-dimensional nanochannels may offer new opportunities for manipulating nanoscale chemical transformation, mass transportation, and wave propagation.

INTRODUCTION

Colloidal crystals are ordered superstructures of colloidal particles whose repeating subunits are much larger than their analogous atomic and molecular crystals (*1*–*4*). The spatial configuration of matter and surface ligands in colloidal crystals, which control many physical and chemical properties, can be tailored in a nanometer precision by adjusting the subunit composites, sizes, shapes, and crystal structures (*5*–*8*). Therefore, the colloidal assembly has become an effective strategy in producing many functional materials in photonics (*9*–*12*), structural materials (*13*, *14*), robotics (*15*–*17*), and catalysis (*18*, *19*). The assembly of either spherical or highly faceted colloids is mainly dominated by entropic processes that involve depletion, hydrophobic forces, and polymer "elasticity," producing densely packed colloidal crystals with close surface contact (*3*, *20*, *21*). Theoretical simulations and colloidal self-assembly at multiscale have demonstrated this common assembly manner (*22*–*24*).

For exploring more complex superstructures, sole or joint anisotropic interactions have been introduced (*25*), including specific binding between biomolecules (particularly DNA) (*26*–*29*), van der Waals forces of ligands (*1*, *30*), magnetic forces (*31*–*33*), and electrostatic forces (*3*, *34*, *35*). A few advanced strategies use directed interactions between Janus microparticles for creating emerging superstructures (*36*–*40*). Among these established methods, the nanoscale magnetic assembly provides precise control over colloidal crystal symmetry and orientation, and the dynamic interplay between magnetic forces and other underlying forces of different length scales offers great opportunities in creating emerging superstructures and smart materials. A great benefit in this regard is the widely accessible range of monodisperse magnetic colloids with defined shapes, tunable properties, and delicate structures. Scientists are achieving even more exquisite control over the synthesis of magnetic particles, including those with various shapes (*41*–*44*), core/shell nanoparticles (*45*–*47*), and Janus particles with magnetic patches (*39*, *48*, *49*), setting the stage ready for exploiting their assembly into complex superstructures with remarkable collective properties. In this work, we demonstrate that body-centered tetragonal (bct) superstructures with reduced crystal symmetry can be developed by the magnetic assembly of nanorods in colloidal solutions. It has been known since 1269 that opposite magnetic poles attract, favoring dipole-to-dipole end-on attachment (*50*). At the nanoscale, however, magnetic nanorods assemble along a size-dependent critical angle. The shape-induced anisotropic interaction generates two attractive domains separated by a magnetically repulsive center domain. It directs nanorods to assemble along the critical axis into bct crystals, rather than the side-on attachment favored in entropy-dominated assembly or end-on attachment favored by magnet opposite pole attraction. A simple extension of the nanoscale magnetic assembly to different nanorods yields bct crystals with tunable lattice constants, tailorable physical properties, readily accessible surfaces, and interconnected nanochannels.

RESULTS

FeOOH nanorods (aspect ratios from 3 to 30) were synthesized by hydrolysis of $FeCl_3$ (figs. S1 and S2 and table S1) and further reduced to magnetic nanorods after being coated with silica of controllable thickness (fig. S3) (*43*, *51*). In this surface-protected reduction, the silica shell maintains the rod shape during the phase transition of FeOOH to Fe_3O_4 and alleviates the considerable volume shrinkage. A transmission electron microscopy (TEM) image in Fig. 1A reveals the high uniformity of the magnetic rods (322 nm by 70 nm). The magnetic assembly was performed by simply sitting a rod dispersion above a permanent magnet with a field strength of 150 mT. As shown in Fig. 1 (B and C) and fig. S4, stripe-like, green crystals formed. The scanning electron microscopy (SEM) image in Fig. 1C reveals that the magnetic nanorods are packed into a centered rectangular lattice on the crystal surface. The apparent orthogonality and different periodicity between transverse and longitudinal directions demonstrate the reduced symmetry of the

[1]Department of Chemistry, University of California, Riverside, CA 92521, USA. [2]Advanced Light Source, Lawrence Berkeley National Laboratory, 1 Cyclotron Rd., Berkeley, CA 94720, USA.
*Corresponding author. Email: yadong.yin@ucr.edu
†Present address: Department of Materials Science and Engineering, University of Illinois at Urbana-Champaign, Urbana, IL 61801, USA.

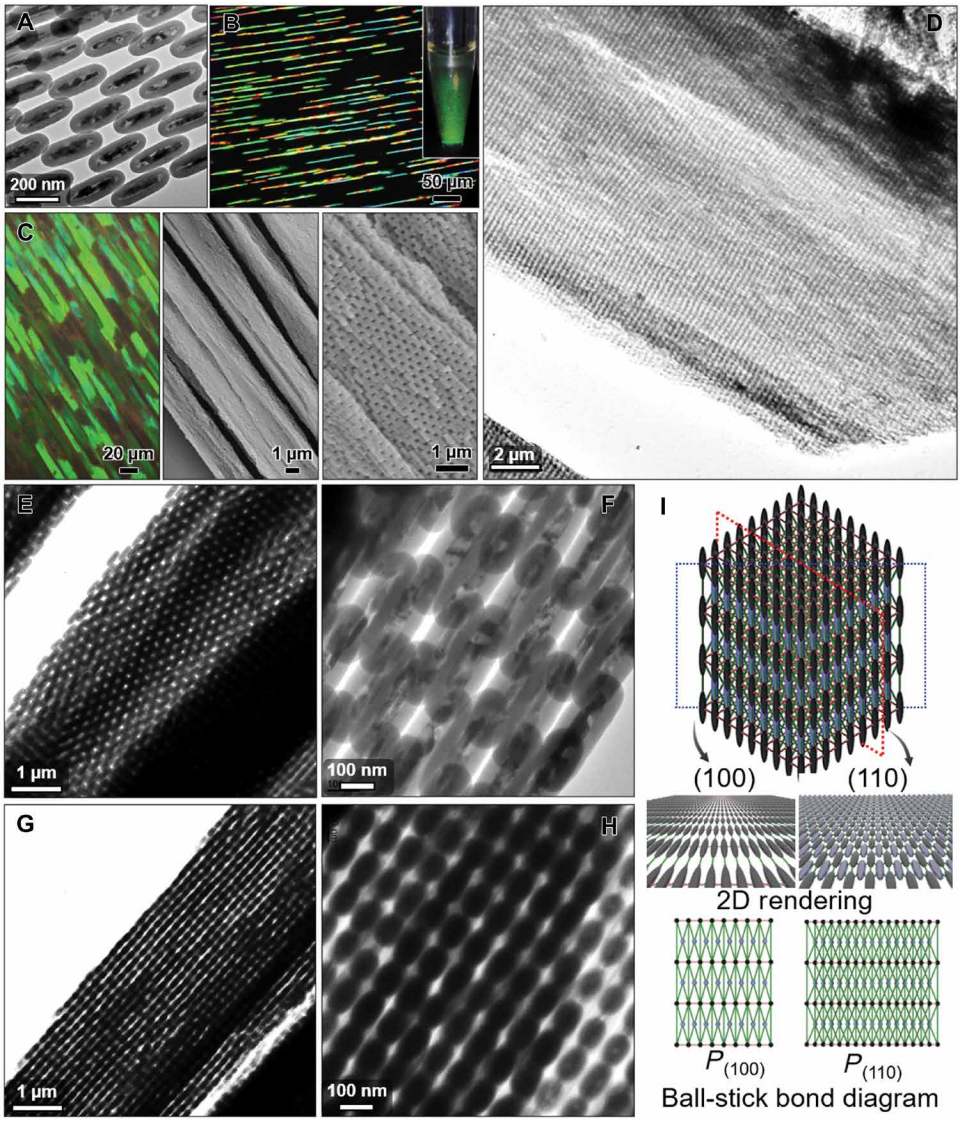

Fig. 1. Magnetic assembly of nanorods into bct colloidal crystals. (**A**) TEM image of Fe_3O_4@SiO_2 nanorods. (**B**) Dark-field optical microscopy image of the needle-like colloidal crystals under an external magnetic field. Inset shows a digital photo of a rod dispersion in a vertical magnetic field. (**C**) Left: Optical microscopy image of the colloidal crystals in a colloidal dispersion. Middle to right: Low-magnification SEM image showing the fixed needle-like structures and high-magnification SEM image showing the characteristic rod packing on the crystal surfaces. (**D**) Low-magnification TEM image of assembled hollow SiO_2 ellipsoids formed by postassembly etching of Fe_3O_4 core. (**E** to **H**) TEM images of the assembled crystals under the projections of different crystal facets. (**I**) The 3D reddening and ball-stick bond diagram of the bct colloidal crystal and its facets.

crystals and exclude any triclinic, monoclinic, or cubic crystal systems. These observations suggest a few possible Bravais lattices, including body-centered orthorhombic, face-centered orthorhombic, and bct structures.

The silica fixation allows the colloidal crystals to be transformed into other colloid lattices by postassembly wet chemical processes. For example, selectively etching away Fe_3O_4 yields crystals of SiO_2 shells (Fig. 1D). In a two-dimensional (2D) projection, the contact joints between neighboring rods form high-density areas (dark regions in the 2D projection) separated by low-density, low-contrast domains (figs. S5 to S7). The projection of the assembled crystals along different crystallographic directions produced characteristic 2D TEM images, with two typical lattices being observed, rectangular phase (Figs. 1E and 2F) and centered rectangular phase (Fig. 1, G and H). In Fig. 1E, the periodic empty spaces indicate that the rods are in hard contact but not closely packed. Crystals sharing this characteristic projection have identical transverse periodicity. These observations approve that the assembled structures are bct crystals because the hard contact between neighboring rods and the same transverse periodicity do not support the different interplanar spacing of (100) and (010) facets in orthorhombic crystals. A high-magnification image of the same area reveals overlaps of rod ends, creating defined joints and interconnected nanometer poles (Fig. 1F). In Fig. 1 (G and H), we observed layer-by-layer stacking of crystal planes with apparent periodic nodes due to the partial rod overlap. The projection of rod packing along this crystallographic

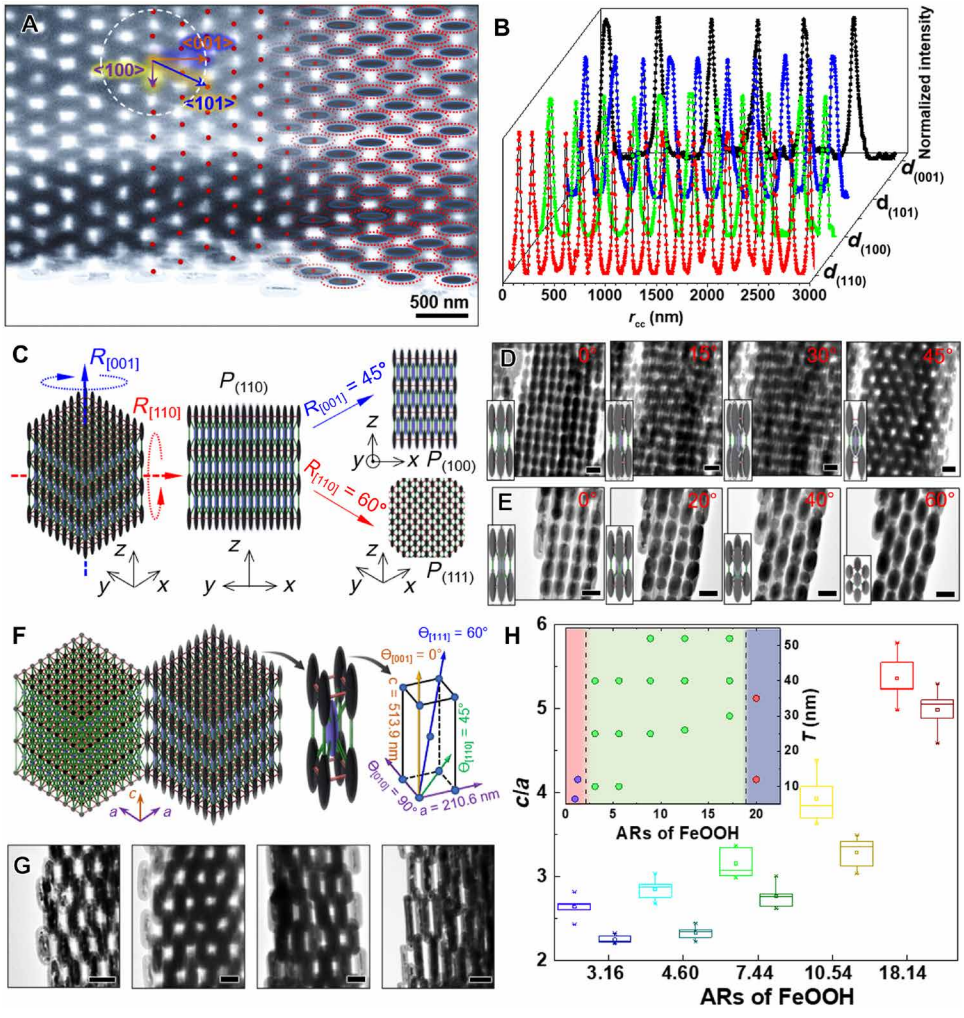

Fig. 2. Structure characterization of bct colloidal crystals. (**A**) TEM image of the bct crystal showing the projection of (100) facets. Positions of rods are identified and mapped to a bct lattice. (**B**) Normalized distribution intensity of nanorods inside the crystals in (A) along different crystallographic directions. (**C**) Schematics of bct crystals under different orientations by rotating along given crystallographic directions. TEM images in (**D**) and (**E**) show bct crystals under various orientations by rotating along [001] and [110], respectively. (**F**) Simulated bct colloidal crystals. (**G**) TEM images of bct crystals assembled from magnetic nanorods with different sizes and aspect ratios. (**H**) The dependence of lattice constant ratio (*c*/*a*) on the aspect ratios (ARs) of magnetic nanorods. Inset is the experimental phase diagram showing the magnetic assembly behaviors of rods. Blue, green, and red dots represent linear colloidal chains, bct crystals, and disordered fibers with only orientational orders, respectively. Scale bars in (D), (E), and (G) are 200 nm.

direction is a rectangular 2D lattice. The arrangements of rods in the two typical planes are illustrated in the 2D rendering (Fig. 1I). The rods packing in (110) facets is consistent with the SEM images in Fig. 1C. The projection patterns (ball-stick bond diagram in Fig. 1I) of (100) and (110) facets are consistent with TEM images in Fig. 1 (E and F), respectively.

The rod positions in the crystals are identified and mapped in Fig. 2A. Their radical distribution (r_{cc}) in Fig. 2B demonstrates the excellent orders and defines the lattice spacing (d) of (110), (100), (101), and (001) facets. The 3D rod arrangement and the crystal rotational symmetry were systematically studied by electron tomography (movie S1). In Fig. 2C, we started with a projection of (110) facets, $P_{(110)}$, and acquired TEM images by continuously rotating crystals along [001] and [110] crystallographic directions, denoted as $R_{[001]}$ and $R_{[110]}$, respectively. The initial $P_{(110)}$ exhibits a layer-by-layer structure with a centered rectangular rod packing in (110) facets (Fig. 2D). When $R_{[001]}$ = 45°, we observed a gradual evolution to $P_{(100)}$, with rectangular rod arrangements in (100) facets. In $R_{[110]}$, the initial $P_{(100)}$ transforms to $P_{(111)}$ when the tilting angle increased to 60°, leading to a rectangular out-of-plane topography of rods (Fig. 2E). A 3D rendering model and ball-stick bond diagram are illustrated in Fig. 2F. In a unit cell, eight rods occupy the vertex sites, with one in the center, forming a bct lattice. Its length along the *a* and *c* axes is 210.6 and 513.9 nm, respectively. The angle between [111] and [110] is 30°. Using nanorods with different sizes and silica thicknesses, we obtained several bct colloidal crystals with tunable critical angles, lattice constants, and packing densities (figs. S8 to S14). In Fig. 2G, projections of (100) crystal facets are obtained with rod aspect ratio increasing from 2.25 to 18.5. Because of the dipole-dipole attractions, isotropic nanospheres were assembled into 1D nanochains (*52*, *53*). In the phase diagram (Fig. 2H, inset), long nanorods (aspect ratio, >20) self-assembled into disordered fibers largely because of the segregation of magnetic cores during reduction.

For Fe_3O_4@SiO_2 colloids with abundant surface charges, the electrostatic repulsion is a major counterforce to the magnetic attraction (*54*). Its classic use involves the multipolar expansion of an analytical equation, whose direction is mainly along the connecting line of interacting colloids. The monopole approximation is operational for isotropic, homogeneously charged spheres (fig. S15) or anisotropic colloids with considerably large separation (*55*). As colloids approach, their morphological anisotropy becomes more effective. Our finite element analysis (fig. S16) points out that the electrostatic repulsion is highly dependent on interparticle separation and that, in closely packed assemblies, it gradually approaches the surface normal of interacting rods. At thermodynamic equilibrium, the tangent component of the magnetic attraction is expected to vanish to avoid any relative translational shifts between nanorods, and the normal component is balanced by the electrostatic and steric repulsion. For understanding the force dynamics, one nanorod (in red color in Fig. 3A) is continuously swept along a defined trajectory in hard contact with a primary rod (in blue color). The magnetic force between them is dependent on silica thickness (t) and azimuth angle (θ) (fig. S17 and movie S2). To identify the critical angles (ϕ_c) along which interacting rods thermodynamically equilibrate, we decompose the overall magnetic force into tangent (F_{tang}) and normal components (F_{norm}). In Fig. 3B, F_{norm} changes from negative to positive values at θ = 43°, which defines the repulsion and attraction domains, respectively. In the attraction regime, we specify a critical point at F_{tang} = 0, where the magnetic attraction is along the surface normal. For 50-nm silica shells, the theoretical ϕ_c is 68.1°, and its good agreement with the measured value of 63.5° from TEM images appreciates the reasonable accuracy of this simple calculation. The normal component in Fig. 3C (right) demonstrates the presence of the two attractive poles and the repulsive center, with their boundary shifting to small θ regions as silica thickness increased from 5 to 50 nm. We observed the first decrease and then increase in ϕ_c in the attractive domain (dashed blue line in Fig. 3C, left). To understand the deterministic role of aspect ratios, we analyzed ϕ_c for different magnetic rods and map their ϕ_c in a 3D surface in Fig. 3D. For isotropic nanospheres, ϕ_c remains 90° due to the dipole-dipole attraction, producing 1D chains with end-on attachment (figs. S18 and S19). Anisotropic nanorods favor offset packing with a defined ϕ_c, which lastly degenerate to 90° as the SiO_2 thickness increases. The ϕ_c increased as aspect ratios simply because of rod elongation (figs. S20 to S27).

The offset binding between two rods initiated the nucleation of bct crystals as neighboring rods assemble at preferential crystalline

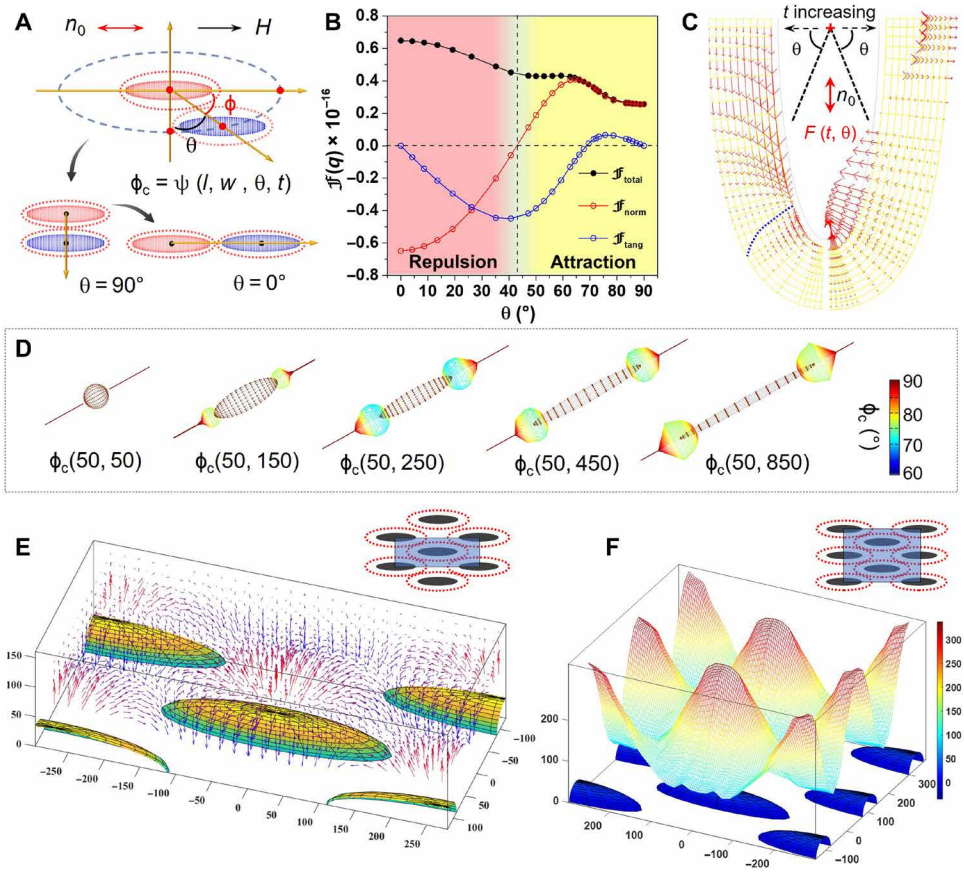

Fig. 3. Assembly mechanism and force dynamics. (**A**) Schematics showing the geometry for calculating the pair interaction between two nanorods under a horizontal magnetic field. (**B**) Plot of total force and its normal, tangent components against θ when SiO_2 thickness is 50 nm. (**C**) Force field of the normal (left half) and tangent (right half) components of the pair interactions between two magnetic nanorods (t = 50 nm) by varying separation and angles (θ) between r_{cc} and n_0. (**D**) 3D mapping of critical angles (ϕ_c) for nanorods with different aspect ratios. (**E**) 3D force fields of magnetic interactions experienced by one nanorod above the 2D assemblies. (**F**) Magnetic potential above the 2D assemblies at certain separations.

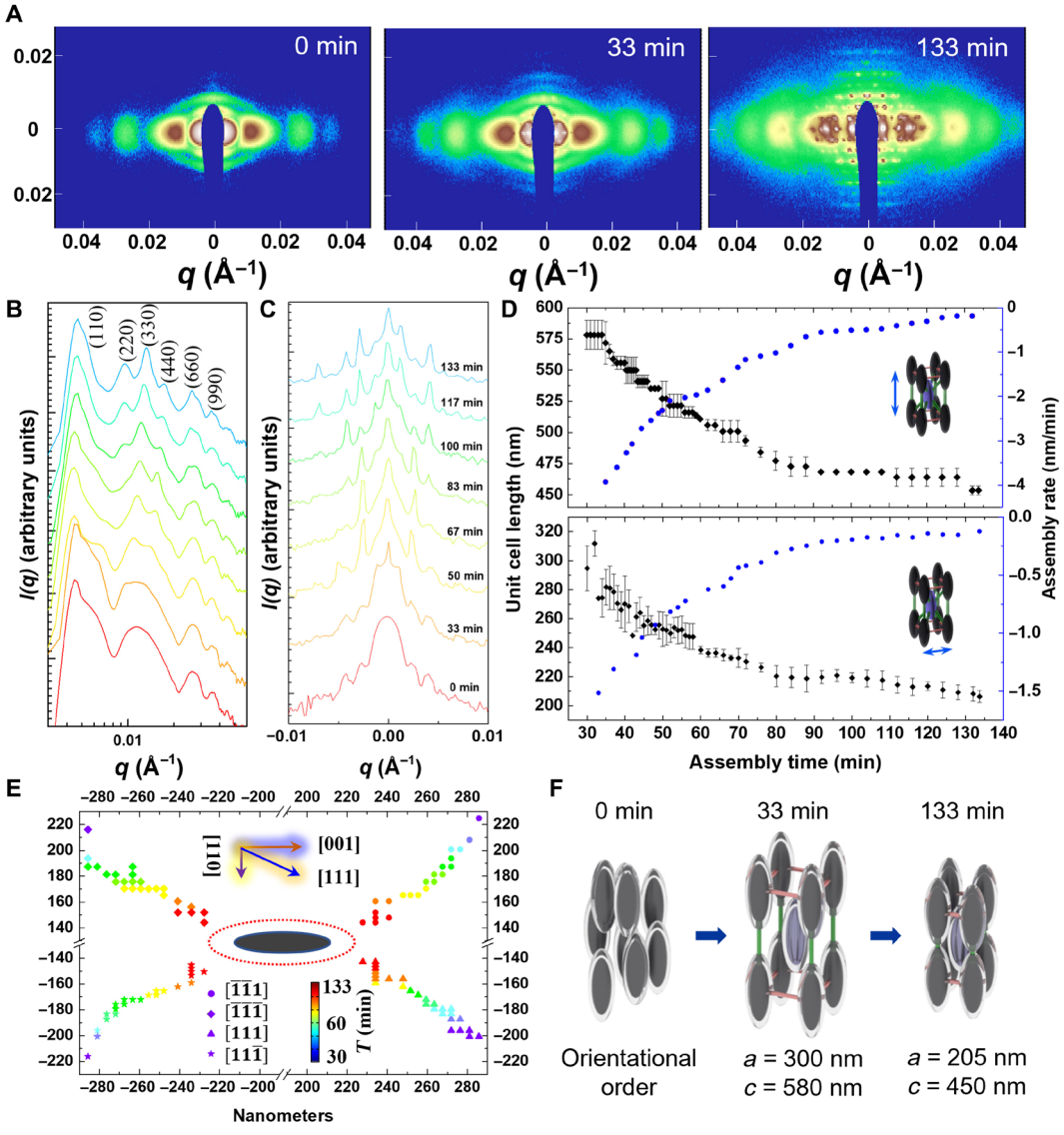

Fig. 4. Assembly kinetics. (**A**) Temporal evolution of SAXS patterns during the in situ measurement of magnetic assembly of nanorods. (**B** and **C**) Representative linear profile of SAXS patterns along the horizontal (B) and vertical (C) directions. (**D**) Magnetic assembly kinetics of the bct crystals along the *c* axis (top) and the *a* axis (bottom). (**E**) The trajectory of the magnetic nanorods during the assembly process. (**F**) The depiction of the magnetic assembly and formation of bct crystals.

sites along a predicted critical angle. It likely breaks the lateral symmetry of rods, creating a few preferred sites for rod deposition. The crystal growth features preferential in-plane rod tessellation in {110} facets, as evidenced by contrast differences in TEM images; the uniform contrast of TEM images along <110> projection (fig. S28, B to D) implies even, sequent rod packing in the exposed (110) facets. Along <100> (fig. S28, E to G) projections, a contrasting gradient implies a gradual decrease in crystal thickness from crystal center to edge. These observations suggest a defined rectangular cross section of bct crystal grains (fig. S28A) and the preferential in-plane rod packing in (110) facets. While the critical angle analysis demonstrates the offset packing of interacting nanorods, the formation of 3D tetragonal crystals requires higher-dimensional analysis of the assembly dynamics. We extended the force computation to a 3D model (figs. S29 to S32 and movie S3). The force field in Fig. 3E suggests a strong repulsion (red arrows) when the rod overlaps the bottom ones. We observe a gradual shift to a strong attraction when the rod moves to positions above cavities (blue arrows). In the magnetic potential landscape (Fig. 3F), we recognize periodic bonding sites above bottom cavities due to the localized low magnetic potential. There exist four active sites above and below each rod in the 2D sheet, resulting in eight bonded rods shared by its neighbors.

To resolve the assembly kinetics, we analyzed the crystallization by in situ synchrotron-based small-angle x-ray scattering (SAXS) based on the geometry shown in fig. S33 (*56*). The representative 2D SAXS patterns are shown in Fig. 4A, fig. S34, and movie S4. At 0 min, the anisotropic scattering pattern implies the liquid crystal phase of rods with only orientational orders and parallel alignment to a vertical magnetic field. At 33 min, a defined rectangular diffraction pattern appeared as nanorods began to crystalize, which is the reciprocal lattice of {110} facets (fig. S35). The high-order diffraction peaks confirm the perfect structures of the bct crystals. For

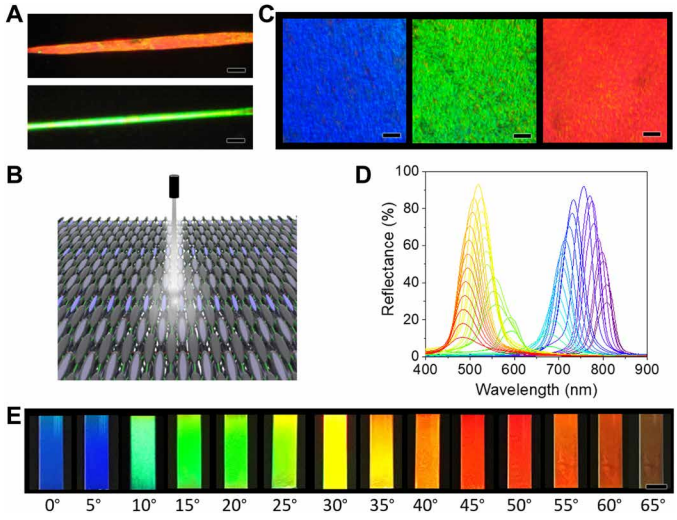

Fig. 5. Optical properties of the assembled bct photonic crystals. (**A**) Optical microscopy images of a bct crystal under different orientations. (**B**) Schematic illustration of measuring the crystal optical properties. Light was incident along the surface normal, and a horizontal (0°) magnetic field was applied. (**C**) Optical microscopy images of the bct crystals under different magnetic field directions: blue at 0°, green at 20°, and red at 45°. (**D**) Measured reflection spectra of rod dispersion under different magnetic fields. Increasing the field direction from 0° to 65° leads to a gradual red shift of the reflection peaks. (**E**) Structural colors of rods dispersion under different magnetic fields. Scale bars, 20 μm (A and C) and 5 mm (E).

example, the linear profiles in Fig. 4 [B (horizontal) and C (vertical)] show a ninth diffraction of {110} facets and fifth diffraction of {001} facets, respectively. Figure 4D represents a time-dependent contraction of the lattice under external magnetic fields with exponential superlattice densification. The lattice contraction rate along both the *a* and *c* directions was initially at ~4 nm/min and slowed down when approaching thermodynamic equilibrium at ~90 min. The considerably slow assembly kinetics provide rods with sufficient spatiotemporal degrees of freedom to anneal out defects. Figure 4E shows the evolution of local rod position along <111> crystallographic directions, indicating nearly linear spatial lattice contraction (fig. S36). The overall magnetic assembly was compiled and depicted in Fig. 4F with lattice shrinkage of 31.7 and 22.4% for the *a* and *c* axes, respectively.

The bct crystals exhibit brilliant structural colors that are dependent on crystal orientation (movie S5). In the dark-field optical microscopy images in Fig. 5A, we observed structural colors diffracted from two types of facets: red from {100} and green from {110} facets. The uniform structural colors elucidate the good crystallinity of the superstructures. The incident light was kept vertical along the crystal surface for measuring the angle-dependent optical properties (Fig. 5B). A horizontal magnetic field (0°) was applied, and spectra were measured by gradually changing the field to the vertical direction (90°). The three primary colors, blue, green, and red, can be observed at 0°, 20°, and 45°, respectively (Fig. 5C). The diffraction spectra in Fig. 5D further demonstrated a gradual red shift of the diffraction peaks due to the increasing periodicity when the crystal orientation increased to 90°. Their diffraction could cover the whole visible range from blue to cyan, green, yellow, orange, and, lastly, red by simply changing the magnetic field directions (Fig. 5E and movies S6 and S7). A simple extension to different nanorods yields photonic crystals with tunable lattice constants and structure colors (fig. S37).

DISCUSSION

In summary, we report the magnetic assembly of magnetite nanorods into tetragonal colloidal crystals and show that the magnetic nanorods assemble along a size-dependent critical angle rather than the simple end-on attachment. The coupled shape and magnetic anisotropy in nanorods is responsible for the unconventional assembly manner and leads to the non–close-packed and hard-contact phase. The unique 3D tetragonal architectures and tunable, interconnected porosity provide a unique platform to modulate many chemical transformations and physical processes in energy conversion and optical devices. This work demonstrates that manipulating magnetic interactions of various anisotropically shaped nanostructures can break the limitation of the dense packing phase in the conventional entropy–dominated colloidal assembly systems, thereby opening the door to creating many complex colloidal crystals.

MATERIALS AND METHODS

Synthesis of FeOOH nanorods

The synthesis of nanorods with different aspect ratios was achieved by hydrolysis of $FeCl_3$ in an aqueous solution (*57*, *58*). The details about the concentration and reaction temperature are summarized in table S1. The synthesis of FeOOH nanorods with small aspect ratios was carried out at room temperature without HCl. Because of relatively low temperature, it takes about 3 months for the formation of uniform FeOOH nanorods. To synthesize FeOOH nanorods with larger aspect ratios (fig. S2), we added HCl to the solution and raised the reaction temperature to 87°C. The reactions were kept at this temperature for 25.5 hours. Notably, this hydrolysis method can be easily scaled up without a significant change in size and aspect ratios. In the example of rods with aspect ratios of 4.6 (#F2), the total volume was 4 liters during room temperature hydrolysis. The concentration of $FeCl_3{\cdot}6H_2O$ is 0.04 M. During the reaction, the formed FeOOH nanorods precipitated to the bottom of the reaction containers. After removing the supernatants, the FeOOH nanorods were washed by water three times and then dispersed in 400 ml of water, which served as stock solutions.

PAA modification

For polyacrylic acid (PAA) modification, 3 ml of the stock solution with a theoretical concentration of 90 mg/ml was added into 120 ml of PAA solution (43.2 mg) and stirred for 8 hours. Excess PAA was removed by centrifugation and washing with water three times. The FeOOH-PAA was further dispersed in 9 ml of water for SiO_2 coating.

SiO_2 coating

In a typical coating process, 3 ml of FeOOH-PAA dispersion was added into a flask. The mixture was sonicated for 3 min to fully disperse the rods after 1 ml of ammonia solution was added. Then, 20 ml of ethanol was added to the dispersion. To control the thickness of silica, we added different volumes of tetraethyl orthosilicate (TEOS) to the mixture. In #F2, for example, 30 and 100 μl of TEOS were added to the mixture to achieve thicknesses of 20.5 and 44.2 nm, respectively, after a 30-min reaction. For thicker silica (~72.8 nm), two batches of 130 μl of TEOS were added to the mixture each

30 min to prevent the formation of free silica nanoparticles. Half an hour after the second addition, the FeOOH@SiO_2 nanorods were precipitated by centrifugation and further washed three times by water.

High-temperature reduction

Magnetic nanorods were synthesized by reduction of FeOOH@SiO_2 nanorods in high-temperature calcination. FeOOH@SiO_2 nanorods were dried in crucibles and placed in a tubular furnace (fig. S3). The system was degassed for 10 min by forming gas (5% H_2 and 95% N_2). The reduction occurred at 360°C for 2 hours. After cooling down to room temperature, the prepared Fe_3O_4@SiO_2 nanorods were fully dispersed in water by sonication and then washed by water three times. To further increase the surface charges and facilitate the fixation of colloidal crystals by silica coating, the Fe_3O_4@SiO_2 nanorods were modified by PAA (20 ml, 5 mg/ml) overnight.

Magnetic assembly of nanorods into tetragonal crystals

The assembly of colloidal crystals took place in aqueous dispersions of Fe_3O_4@SiO_2 nanorods (fig. S4). The dispersion was vertically placed above the center of a permanent magnet. For measuring the diffraction of the crystals, colloidal dispersion of Fe_3O_4@SiO_2 nanorods with an initial volume fraction of ~45% was sealed in a flat capillary. After assembling under the magnetic field, diffraction spectra were measured by continuously varying the directions of the applied magnetic field, and the pictures were also taken at the corresponding angles (Fig. 5C). To fix the assembled crystals, we used a small well of the 96-well plates as the container. In a typical reaction, 25 μl of an aqueous dispersion of Fe_3O_4@SiO_2 nanorods (volume fraction of ~45%) was transferred into the well. Three microliters of ammonia, 100 μl of ethanol, and 10 μl of TEOS were added in sequence. The mixture was sonicated for ~30 s and then placed above a permanent magnet. Additional 3 μl of ammonia was added after 10 min, and the reaction was continued for another 10 min. The precipitated crystals were washed with ethanol three times. During each cycle of washing, the crystals were collected by magnetic separation. Sonication and centrifugation would destroy the fixed crystal structures and therefore are not recommended. The crystals were stored in ethanol for further characterization. The positional order of the colloidal crystals decayed because long nanorods were synthesized in high-temperature hydrolysis, and the relatively fast crystal growth produces widely dispersed particles. More TEM images of the bct crystals are shown in fig. S5. According to the projection patterns, we typically observed two types of crystal orientations. Fixing neighboring rods by silica overcoating imparts considerable mechanical stability to the crystals, as demonstrated by twisting and bending the bct crystals under mechanical forces (fig. S6). Instead of being destroyed, the crystals deformed to release the internal strains, exhibiting interesting, combined states of colloid rigidness and mechanical elasticity.

SUPPLEMENTARY MATERIALS

Supplementary material for this article is available at https://science.org/doi/10.1126/sciadv.abh1289

REFERENCES AND NOTES

1. T. Wang, J. Zhuang, J. Lynch, O. Chen, Z. Wang, X. Wang, D. LaMontagne, H. Wu, Z. Wang, Y. C. Cao, Self-assembled colloidal superparticles from nanorods. *Science* **338**, 358–363 (2012).
2. F. Li, D. P. Josephson, A. Stein, Colloidal assembly: The road from particles to colloidal molecules and crystals. *Angew. Chem. Int. Ed. Engl.* **50**, 360–388 (2011).
3. W. Xu, Z. Li, Y. Yin, Colloidal assembly approaches to micro/nanostructures of complex morphologies. *Small* **14**, 1801083 (2018).
4. Z. Cai, Z. Li, S. Ravaine, M. He, Y. Song, Y. Yin, H. Zheng, J. Teng, A. Zhang, From colloidal particles to photonic crystals: Advances in self-assembly and their emerging applications. *Chem. Soc. Rev.* **50**, 5898–5951 (2021).
5. Z. Li, Y. Yin, Stimuli-responsive optical nanomaterials. *Adv. Mater.* **31**, 1807061 (2019).
6. S. C. Glotzer, M. J. Solomon, Anisotropy of building blocks and their assembly into complex structures. *Nat. Mater.* **6**, 557–562 (2007).
7. S. Sacanna, D. J. Pine, Shape-anisotropic colloids: Building blocks for complex assemblies. *Curr. Opin. Colloid Interface Sci.* **16**, 96–105 (2011).
8. D. V. Talapin, J.-S. Lee, M. V. Kovalenko, E. V. Shevchenko, Prospects of colloidal nanocrystals for electronic and optoelectronic applications. *Chem. Rev.* **110**, 389–458 (2010).
9. J. Ge, Y. Yin, Responsive photonic crystals. *Angew. Chem. Int. Ed.* **50**, 1492–1522 (2011).
10. Z. Li, Q. Fan, C. Wu, Y. Li, C. Cheng, Y. Yin, Magnetically tunable plasmon coupling of Au nanoshells enabled by space-free confined growth. *Nano Lett.* **20**, 8242–8249 (2020).
11. G. von Freymann, V. Kitaev, B. V. Lotsch, G. A. Ozin, Bottom-up assembly of photonic crystals. *Chem. Soc. Rev.* **42**, 2528–2554 (2013).
12. Z. Li, W. Wang, Y. Yin, Colloidal assembly and active tuning of coupled plasmonic nanospheres. *Trends Chem.* **2**, 593–608 (2020).
13. H.-B. Yao, H.-Y. Fang, X.-H. Wang, S.-H. Yu, Hierarchical assembly of micro–/nano-building blocks: Bio-inspired rigid structural functional materials. *Chem. Soc. Rev.* **40**, 3764–3785 (2011).
14. Z. Li, F. Yang, Y. Yin, Smart materials by nanoscale magnetic assembly. *Adv. Funct. Mater.* **30**, 1903467 (2020).
15. Y. Wang, H. Cui, Q. Zhao, X. Du, Chameleon-inspired structural-color actuators. *Matter* **1**, 626–638 (2019).
16. Z. Li, Z. Ye, L. Han, Q. Fan, C. Wu, D. Ding, H. L. Xin, N. V. Myung, Y. Yin, Polarization-modulated multidirectional photothermal actuators. *Adv. Mater.* **33**, 2006367 (2021).
17. Y. Kim, H. Yuk, R. Zhao, S. A. Chester, X. Zhao, Printing ferromagnetic domains for untethered fast-transforming soft materials. *Nature* **558**, 274–279 (2018).
18. G. M. Whitesides, B. Grzybowski, Self-assembly at all scales. *Science* **295**, 2418–2421 (2002).
19. K. Li, K. Wang, W. Qin, S. Deng, D. Li, J. Shi, Q. Huang, C. Fan, DNA-directed assembly of gold nanohalo for quantitative plasmonic imaging of single-particle catalysis. *J. Am. Chem. Soc.* **137**, 4292–4295 (2015).
20. P. F. Damasceno, M. Engel, S. C. Glotzer, Crystalline assemblies and densest packings of a family of truncated tetrahedra and the role of directional entropic forces. *ACS Nano* **6**, 609–614 (2011).
21. W. Han, Z. Lin, Learning from "Coffee Rings": Ordered structures enabled by controlled evaporative self-assembly. *Angew. Chem. Int. Ed. Engl.* **51**, 1534–1546 (2012).
22. P. F. Damasceno, M. Engel, S. C. Glotzer, Predictive self-assembly of polyhedra into complex structures. *Science* **337**, 453–457 (2012).
23. J. Henzie, M. Grünwald, A. Widmer-Cooper, P. L. Geissler, P. Yang, Self-assembly of uniform polyhedral silver nanocrystals into densest packings and exotic superlattices. *Nat. Mater.* **11**, 131–137 (2012).
24. E. V. Shevchenko, D. V. Talapin, N. A. Kotov, S. O'Brien, C. B. Murray, Structural diversity in binary nanoparticle superlattices. *Nature* **439**, 55–59 (2006).
25. Z. Ou, Z. Wang, B. Luo, E. Luijten, Q. Chen, Kinetic pathways of crystallization at the nanoscale. *Nat. Mater.* **19**, 450–455 (2020).
26. R. J. Macfarlane, B. Lee, M. R. Jones, N. Harris, G. C. Schatz, C. A. Mirkin, Nanoparticle superlattice engineering with DNA. *Science* **334**, 204–208 (2011).
27. S. Y. Park, A. K. Lytton-Jean, B. Lee, S. Weigand, G. C. Schatz, C. A. Mirkin, DNA-programmable nanoparticle crystallization. *Nature* **451**, 553–556 (2008).
28. E. Auyeung, T. I. Li, A. J. Senesi, A. L. Schmucker, B. C. Pals, M. O. de La Cruz, C. A. Mirkin, DNA-mediated nanoparticle crystallization into Wulff polyhedra. *Nature* **505**, 73–77 (2014).
29. H. Lin, S. Lee, L. Sun, M. Spellings, M. Engel, S. C. Glotzer, C. A. Mirkin, Clathrate colloidal crystals. *Science* **355**, 931–935 (2017).
30. X. Ye, J. Chen, M. Engel, J. A. Millan, W. Li, L. Qi, G. Xing, J. E. Collins, C. R. Kagan, J. Li, S. C. Glotzer, C. B. Murray, Competition of shape and interaction patchiness for self-assembling nanoplates. *Nat. Chem.* **5**, 466–473 (2013).
31. G. Singh, H. Chan, A. Baskin, E. Gelman, N. Repnin, P. Král, R. Klajn, Self-assembly of magnetite nanocubes into helical superstructures. *Science* **345**, 1149–1153 (2014).
32. R. M. Erb, H. S. Son, B. Samanta, V. M. Rotello, B. B. Yellen, Magnetic assembly of colloidal superstructures with multipole symmetry. *Nature* **457**, 999–1002 (2009).
33. Q. Zhang, M. Janner, L. He, M. Wang, Y. Hu, Y. Lu, Y. Yin, Photonic labyrinths: Two-dimensional dynamic magnetic assembly and in situ solidification. *Nano Lett.* **13**, 1770–1775 (2013).
34. M. Wang, L. He, W. Xu, X. Wang, Y. Yin, Magnetic assembly and field-tuning of ellipsoidal-nanoparticle-based colloidal photonic crystals. *Angew. Chem. Int. Ed. Engl.* **54**, 7077–7081 (2015).

35. M. E. Leunissen, C. G. Christova, A.-P. Hynninen, C. P. Royall, A. I. Campbell, A. Imhof, M. Dijkstra, R. Van Roij, A. Van Blaaderen, Ionic colloidal crystals of oppositely charged particles. *Nature* **437**, 235–240 (2005).
36. Q. Chen, S. C. Bae, S. Granick, Directed self-assembly of a colloidal kagome lattice. *Nature* **469**, 381–384 (2011).
37. A. A. Shah, B. Schultz, W. Zhang, S. C. Glotzer, M. J. Solomon, Actuation of shape-memory colloidal fibres of Janus ellipsoids. *Nat. Mater.* **14**, 117–124 (2015).
38. Q. Chen, J. K. Whitmer, S. Jiang, S. C. Bae, E. Luijten, S. Granick, Supracolloidal reaction kinetics of Janus spheres. *Science* **331**, 199–202 (2011).
39. S. K. Smoukov, S. Gangwal, M. Marquez, O. D. Velev, Reconfigurable responsive structures assembled from magnetic Janus particles. *Soft Matter* **5**, 1285–1292 (2009).
40. A. Walther, A. H. Müller, Janus particles: Synthesis, self-assembly, physical properties, and applications. *Chem. Rev.* **113**, 5194–5261 (2013).
41. Z. Li, M. Wang, X. Zhang, D. Wang, W. Xu, Y. Yin, Magnetic assembly of nanocubes for orientation-dependent photonic responses. *Nano Lett.* **19**, 6673–6680 (2019).
42. Y. Liu, J. Wang, M. Zhang, H. Li, Z. Lin, Polymer-ligated nanocrystals enabled by nonlinear block copolymer nanoreactors: Synthesis, properties, and applications. *ACS Nano* **14**, 12491–12521 (2020).
43. W. Xu, M. Wang, Z. Li, X. Wang, Y. Wang, M. Xing, Y. Yin, Chemical transformation of colloidal nanostructures with morphological preservation by surface-protection with capping ligands. *Nano Lett.* **17**, 2713–2718 (2017).
44. J. Ge, Y. Hu, M. Biasini, W. P. Beyermann, Y. Yin, Superparamagnetic magnetite colloidal nanocrystal clusters. *Angew. Chem. Int. Ed. Engl.* **46**, 4342–4345 (2007).
45. X. Pang, L. Zhao, W. Han, X. Xin, Z. Lin, A general and robust strategy for the synthesis of nearly monodisperse colloidal nanocrystals. *Nat. Nanotechnol.* **8**, 426–431 (2013).
46. X. Pang, Y. He, J. Jung, Z. Lin, 1D nanocrystals with precisely controlled dimensions, compositions, and architectures. *Science* **353**, 1268–1272 (2016).
47. D. Yang, X. Pang, Y. He, Y. Wang, G. Chen, W. Wang, Z. Lin, Precisely size-tunable magnetic/plasmonic core/shell nanoparticles with controlled optical properties. *Angew. Chem. Int. Ed.* **127**, 12259–12264 (2015).
48. Q. Xie, G. B. Davies, J. Harting, Direct assembly of magnetic Janus particles at a droplet interface. *ACS Nano* **11**, 11232–11239 (2017).
49. J. Hu, S. Zhou, Y. Sun, X. Fang, L. Wu, Fabrication, properties and applications of Janus particles. *Chem. Soc. Rev.* **41**, 4356–4378 (2012).
50. P. Peregrinus, *The Letter of Petrus Peregrinus on the Magnet, AD 1269* (Library of Alexandria, 2020), vol. 1.
51. Y. Lu, Y. Yin, B. T. Mayers, Y. Xia, Modifying the surface properties of superparamagnetic iron oxide nanoparticles through a sol–gel approach. *Nano Lett.* **2**, 183–186 (2002).
52. J. Ge, Y. Hu, Y. Yin, Highly tunable superparamagnetic colloidal photonic crystals. *Angew. Chem. Int. Ed.* **46**, 7428–7431 (2007).
53. Y. Hu, L. He, Y. Yin, Magnetically responsive photonic nanochains. *Angew. Chem. Int. Ed.* **50**, 3747–3750 (2011).
54. L. He, M. Wang, J. Ge, Y. Yin, Magnetic assembly route to colloidal responsive photonic nanostructures. *Acc. Chem. Res.* **45**, 1431–1440 (2012).
55. H. N. Lekkerkerker, R. Tuinier, in *Colloids and the Depletion Interaction* (Springer, 2011), vol. 833, pp. 57–108.
56. A. Hexemer, W. Bras, J. Glossinger, E. Schaible, E. Gann, R. Kirian, A. MacDowell, M. Church, B. Rude, H. Padmore, A SAXS/WAXS/GISAXS beamline with multilayer monochromator. *J. Phys. Conf. Ser.* **247**, 012007 (2010).
57. X. Wang, J. Feng, H. Yu, Y. Jin, A. Davidson, Z. Li, Y. Yin, Anisotropically shaped magnetic/plasmonic nanocomposites for information encryption and magnetic-field-direction sensing. *Research* **2018**, 7527825 (2018).
58. Z. Li, J. Jin, F. Yang, N. Song, Y. Yin, Coupling magnetic and plasmonic anisotropy in hybrid nanorods for mechanochromic responses. *Nat. Commun.* **11**, 2883 (2020).
59. J. Ilavsky, Nika: Software for two-dimensional data reduction. *J. Appl. Cryst.* **45**, 324–328 (2012).
60. J. Ilavsky, P. R. Jemian, Irena: Tool suite for modeling and analysis of small-angle scattering. *J. Appl. Cryst.* **42**, 347–353 (2009).

Acknowledgments: Z.L. thanks X. Wang for helpful discussion in nanorod synthesis and Q. Fan in theoretical analysis. This research used beamline 7.3.3 of the Advanced Light Source, which is from DOE Office of Science User Facility under contract no. DE-AC02-05CH11231. Acknowledgment is also made to the Central Facility for Advanced Microscopy and Microanalysis at UCR for help with TEM analysis. **Funding:** This work was funded by NSF, DMR-1810485. **Author contributions:** Conceptualization: Z.L. and Y.Y. Methodology: Z.L. and C.Q. Investigation: Z.L., W.X., and C.Z. Supervision: Y.Y. Writing (original draft): Z.L. Writing (review and editing): Y.Y. **Competing interests:** Y.Y. and Z.L. are inventors on a pending patent related to this work filed by the University of California Riverside (UC case no. 2021-840, filed 25 February 2021). The authors declare that they have no other competing interests. **Data and materials availability:** All data needed to evaluate the conclusions in the paper are present in the paper and/or the Supplementary Materials. Additional dataset used to analyze the critical angles, phase diagram, electrostatic forces, and magnetic forces are available online at https://zenodo.org/record/4950032#.YMqqbvKSk2w.

Submitted 17 February 2021
Accepted 22 July 2021
Published 10 September 2021
10.1126/sciadv.abh1289

Citation: Z. Li, C. Qian, W. Xu, C. Zhu, Y. Yin, Coupling morphological and magnetic anisotropy for assembling tetragonal colloidal crystals. *Sci. Adv.* **7**, eabh1289 (2021).